Chapter 1

Introduction and literature review

1.1 Motivation of thesis

Perovskite oxides are materials with the general formula ABO_3, and have a structure similar to the mineral perovskite, Calcium Titanate ($CaTiO_3$) [5]. This mineral was first discovered by Gustav Rose in 1839 in the Ural Mountains of Russia and was named in honour of the Russian mineralogist L. A. Perovski. Perovskite materials exhibit various fascinating properties such as ferroelectricity, ferromagnetism, ferroelasticity, etc., which are important from a technological point of view [12, 13, 14, 15]. These compounds are used as sensors and actuators in various types of electromechanical devices and form an important ingredient for memory devices [16, 17, 18, 19]. Currently, most of the functional materials that are being used in the industries are lead-based [20, 21, 22, 23]. However, directives regulating Pb and other toxic elements in commercial products (introduced in the EU in the early 21st century) have accelerated interest in developing lead-free functional materials [24, 25, 26, 27].

Crystal structure modification is one of the most effective methods for customizing the physical properties of perovskite oxides. Through this approach, it becomes possible to design materials that either exhibit a phase boundary (coexistence of more than one

ferroelectric phase) or demonstrate relaxor behaviour (polar regions in non-polar matrix), allowing manipulation of functional properties for specific technological applications [9, 28]. Therefore, modification of the long and/or short-range structures is promising for improving the physical properties in perovskite oxides. The two well-studied phase boundaries in the perovskite-based systems are (i) Morphotropic phase boundary (MPB) and (ii) Polymorphic phase boundary (PPB) [29]. While they are different in the sense of thermal stability (MPB is thermally stable in comparison to PPB), they rely on the same physical phenomenon of polarization rotation and extension for maximization of physical response [30]. $PbTi_xZr_{1-x}O_3$ (PZT) is a commonly used lead-based functional material demonstrating MPB for $0.48 \leq x \leq 0.50$ [21, 31]. PZT is a solid solution of orthorhombic $PbZrO_3$ (antiferroelectric, space group: *Pbam*) and tetragonal $PbTiO_3$ (ferroelectric, space group: *P4mm*). To mimic a similar but lead-free candidate, we have synthesized the solid solution of Sodium Niobate ($NaNbO_3$) with Barium Calcium Titanate ($Ba_{0.9}Ca_{0.1}TiO_3$) in order to stabilize inter-ferroelectric phase transitions at ambient conditions resulting in Morphotropic/Polymorphic phase boundary [32, 33, 34, 35]. Here, one of the end members, i.e., $NaNbO_3$ (NN), is characterized by an orthorhombic crystal structure with antiferroelectric (AFE) ordering (space group: *Pbcm*) [36]. In contrast, the $Ba_{0.9}Ca_{0.1}TiO_3$ (BCT) exhibits a tetragonal structure with ferroelectric ordering (space group: *P4mm*) [37]. Furthermore, it has been found that in (Ba, Ca)TiO_3, the ferroactive Ca^{2+} cation promotes off-centering of the B-site (Ti^{4+}) cation (similar to the role of Pb^{2+} in $PbTiO_3$), thereby enhancing ferroelectric polarization. The above discussion makes $Ba_{0.9}Ca_{0.1}TiO_3$ (BCT) analogous to $PbTiO_3$ [38]. It is also reported that inclusion of Ca at A-site in $BaTiO_3$ promotes stable ferroelectric domains and finer grain size, resulting in high dielectric permittivity, low loss, and high polarization [39]. Despite numerous studies on the solid solutions of Sodium Niobate (NN) and Barium Titanate (BT), the detailed crystallographic

analysis remains uncovered, thereby motivating us for a detailed structural analysis(short and long range) using multiple characterization techniques [32, 33, 35, 40, 41, 42].

In light of the above discussion, we have synthesized the lead-free solid solution $NaNbO_3$ - $xBa_{0.9}Ca_{0.1}TiO_3$ (BCT) [NN-xBCT] using a conventional solid-state reaction method. The competitive interaction between the distinct ferroic ordering of NN and BCT may lead to ferroelectric instabilities, resulting in various phase boundaries. Moreover, relaxor-like characteristics can be induced in the present system by tuning the stoichiometric ratio (via creating disorder) of the two end members. Following these ideas, we have identified two distinct polymorphic phase boundaries in 0.9 $NaNbO_3$ (NN) - 0.1 $Ba_{0.9}Ca_{0.1}TiO_3$ (NN-10BCT). Temperature-dependent Synchrotron X-ray diffraction (SXRD) in conjunction with dielectric analysis confirmed the presence of a Polymorphic Phase Boundary (PPB), characterised by the coexistence of two ferroelectric phases, *viz.,* *Amm2* and $Pmc2_1$, in the vicinity of room temperature. The coexistence region of the two phases persists over a broad temperature range ($\Delta T \approx 80$ K). Furthermore, an additional PPB, exhibiting the coexistence of orthorhombic (Space group: $Pmc2_1$) and rhombohedral (Space group: *R3c*) ferroelectric phases, was identified at low temperatures. This low-temperature phase coexistence spans a broader temperature interval (with $\Delta T \approx 190$ K during the heating cycle, and $\Delta T \approx 120$ K during the cooling cycle) in comparison to the PPB observed at ambient conditions. Therefore, this composition may demonstrate potential for cryogenic applications. Furthermore, the relaxor behaviour of compositions with higher BCT content *viz.,* 0.75 $NaNbO_3$ - 0.25 $Ba_{0.9}Ca_{0.1}TiO_3$ (NN-25BCT) and 0.40 $NaNbO_3$- 0.60 $Ba_{0.9}Ca_{0.1}TiO_3$ (NN-60BCT), has also been investigated. NN-25BCT exhibits a relaxor-to-ferroelectric phase transition near room temperature, making it a promising candidate for applications in pyroelectric detection and electrocaloric devices. In contrast, NN-60BCT behaves as a canonical relaxor, which does not transform into a ferroelectric state at low temperatures (below T_{VF}). However, due to the enhanced corre-

lations among polar nano-regions (PNRs), NN-60BCT demonstrates anomalous thermal expansion (commonly referred to as the ferroelectrovolume effect) at low temperatures. Moreover, NN-60BCT can be used as a model system for investigating the unusual thermal expansion behaviour observed in relaxor ferroelectrics. Therefore, this thesis work highlights the influence of the long- and/or short-range structural ordering on the physical properties of a lead-free perovskite-based system.

1.2 Physical hierarchy of some functional material

Functional materials exhibit unique physical properties that make them essential for various technological applications, including energy storage, sensing, and actuation [43]. Among these, dielectric, piezoelectric, pyroelectric, and ferroelectric materials form a well-defined physical hierarchy, each possessing distinct characteristics and applications [5]. The relationship between these materials can be understood using the Venn diagram shown in Fig. 1.1 The essential properties of these material classes are outlined as follows:

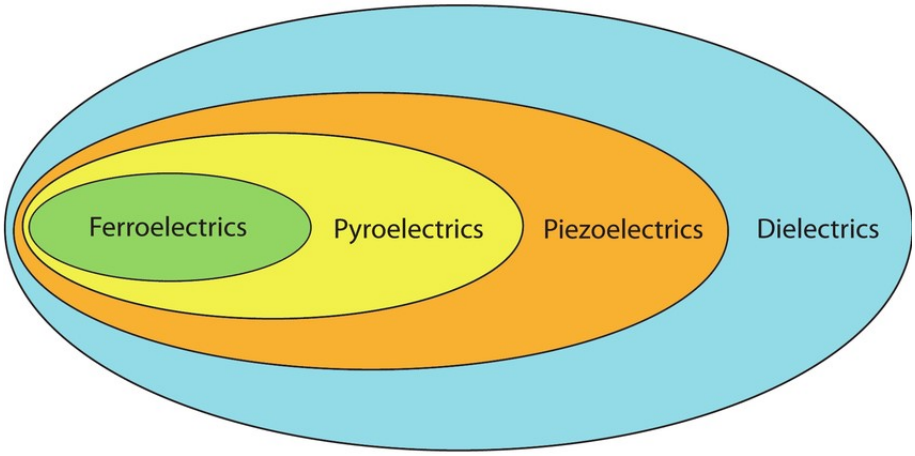

Fig. 1.1 The relationship between the piezoelectric, pyroelectric, and ferroelectric materials.

1.2.1 Dielectrics

The dielectric characteristics of insulating materials originate from the presence of polarizable elements within their crystal structure [18]. These include displacement of cations as well as intrinsic defects such as point defects and grain boundaries [44]. The fundamental parameter characterizing a dielectric is its relative permittivity. In a static electric field, it is denoted as ε'. However, under an alternating electric field, it is expressed as the **complex relative permittivity**, given by:

$$\tilde{\varepsilon} = \varepsilon' - i\varepsilon'' \tag{1.1}$$

which varies with the frequency of the applied field. An important parameter describing dielectric behaviour in a varying electric field is the **energy loss**, commonly represented by the **loss tangent** ($\tan\delta$) and defined as:

$$\tan\delta = \frac{\varepsilon''}{\varepsilon'} \tag{1.2}$$

The dielectric properties of crystalline solids are highly influenced by the microstructure of the material, such as the grain size, porosity, voids within the material, and/or the presence of any impurity phases [9]. Additionally, chemical defects like mobile charge carriers and point defects inside grains, as well as the physical and chemical nature of grain boundaries, all impact the observed properties of the solid. As a result, a controlled fabrication process with optimized temperature and dwell time is highly required to tailor the dielectric properties of the material.

1.2.2 Piezoelectrics

The term "Piezo" is derived from the Greek language and translates to "Pressure". Some dielectric materials generate electric charges on their surface when subjected to mechanical stress (see Fig. 1.2). The charge hence produced is directly proportional to the magnitude

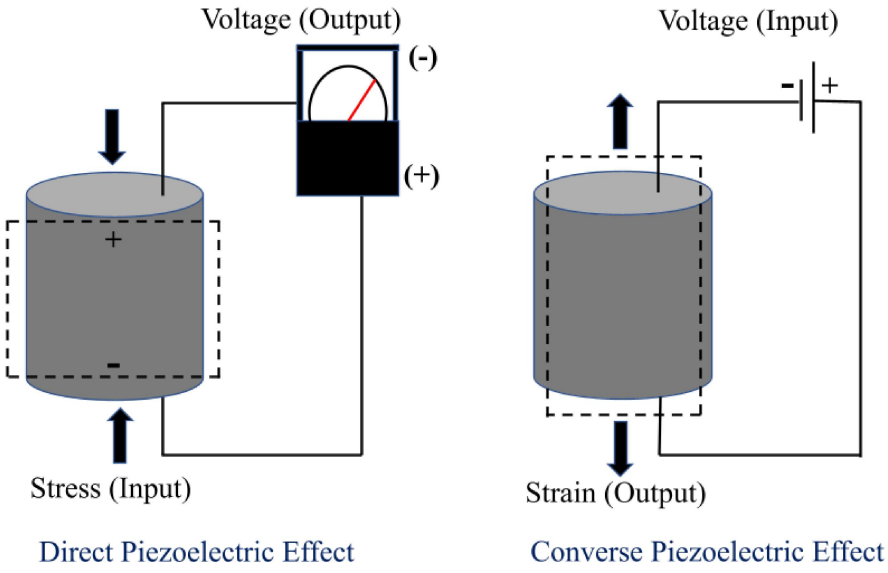

Fig. 1.2 Representation of direct and converse piezoelectric effect.

of the applied stress. This phenomenon is termed as the direct piezoelectric effect, and materials that display this behavior are called piezoelectric materials [28]. Pierre and Jacques Curie first discovered this effect in quartz in 1880. From a crystallographic point of view, a piezoelectric material must be non-centrosymmetric. This phenomenon is usually quantified by the piezoelectric coefficient (d), which is defined as the ratio of charge per unit area (polarization) and applied stress

$$P = \frac{Q}{A} = dX \tag{1.3}$$

where Q is the charge, P represents polarization, and A is the surface area of the sample. This effect is reversible, meaning that applying an electric field can also induce mechanical strain in the material. The induced strain is directly proportional to the applied electric field, and their relationship is expressed as:

$$x = d\,E \tag{1.4}$$

where x represents the induced strain, E is the applied electric field, and d denotes the piezoelectric constant. Notably, d is a third-rank tensor quantity. These materials are important ingredients for fabricating various devices, including actuators, sensors, surface acoustic wave (SAW) devices, and so on [28, 45, 46].

1.2.3 Pyroelectrics

Pyroelectric materials exhibit spontaneous polarization that changes with temperature, resulting in the generation of an electric charge [17]. Since pyroelectric materials must be polar and exhibit a certain degree of polarization, they essentially possess piezoelectric properties. Therefore, pyroelectrics form a subclass of piezoelectric materials, i.e., all pyroelectric materials are also piezoelectric [47, 48, 49]. The magnitude of spontaneous polarization depends on temperature and decreases as temperature increases, as higher thermal vibrations disrupt dipole alignment. Conversely, the dipoles realign as the pyroelectric material cools, causing an increase in the number of free charges bound to the surface of the material. In both scenarios (heating or cooling), creating a short circuit allows an electric current to flow through the circuit. This current is known as the Pyroelectric current (i_p). In a short circuit condition, the relationship between pyroelectric charge (Q), generated current (i_p), the surface area of the material (A), rate of temperature change (dT/dt), and pyroelectric coefficient (p) can be written as [49]:

$$i_p = \frac{dQ}{dt} = pA\frac{dT}{dt} \tag{1.5}$$

Despite being a vector quantity, the pyroelectric coefficient is frequently considered a scalar in measurements because the electrodes used for charge collection are generally aligned perpendicular to the polar direction. The sensitivity of pyroelectric materials to small temperature variations has been effectively utilized in infrared imaging and motion

detection based on body heat. Additionally, this small electric current holds potential for energy harvesting applications [50].

1.2.4 Ferroelectrics

Ferroelectrics got their name due to an analogy with ferromagnetism. The prefix "ferro-" comes from the Latin word for iron, as ferromagnetism was initially observed in iron and iron-based materials. A material is classified as ferroelectric if it exhibits spontaneous polarization that can be reversed on the application of an appropriate electric field [18, 51]. Ferroelectricity was first observed in Rochelle salt by Valsek in 1921. In its natural state, a ferroelectric crystal comprises a collection of coherent domains, where the internal electric dipoles within each domain are parallel to one another but are not aligned with those in adjacent domains. The fundamental cause of ferroelectricity in the perovskite oxides (ABO_3) is the off-centred displacement of the B-site cation from its centrosymmetric position. The displaced B-site cation creates an electric dipole within the unit cell. The direction of dipoles can be shifted between different off-centre positions on the application of an applied electric field [5]. A sufficiently strong external electric field opposing the internal dipoles can force the cations to switch to the opposite orientation [5]. This scenario can be depicted using the potential energy of the crystal (see Fig. 1.3). In the potential energy curve, each stable configuration corresponds to one of the minima in the potential energy versus position curve, with a small energy barrier (ΔU) separating them. If the applied electric field is sufficiently strong to surpass the energy barrier, the dipoles will rearrange, which results in a shift between stable configurations.

The switching of domains between the stable configurations can be visualized using the polarization (P) versus electric field (E) loop (Hysteresis) for the ferroelectric material shown in Fig. 1.4. There are three important points on a ferroelectric hysteresis loop:

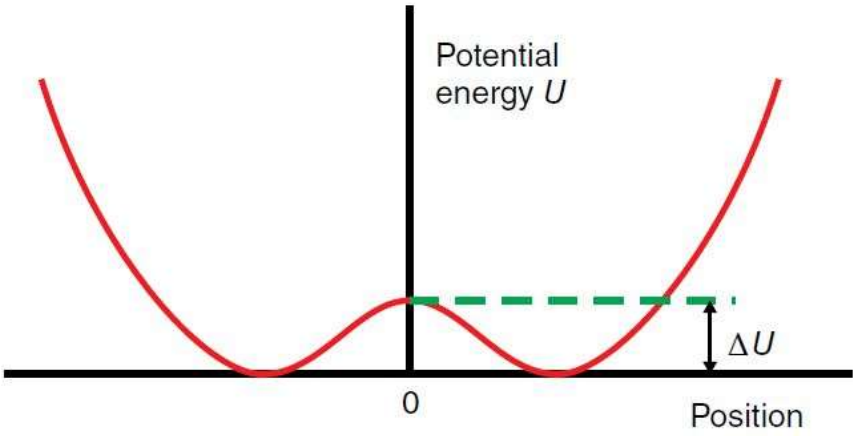

Fig. 1.3 Potential energy curve for a ferroelectric material.

- **Electric Coercivity** (E_C): The electric field strength required to reverse polarization between positive and negative states.

- **Remnant Polarization** (P_r): Residual polarization that remains in the material after the external electric field is removed.

- **Saturation Polarization** (P_S or P_{max}): Maximum polarization a material can attain under a strong applied electric field.

As the temperature increases, the thermal motion of atoms increases, eventually surpassing the energy barrier that separates different orientations of spontaneous polarization. At sufficiently high temperatures, atomic positions become randomly distributed, causing the crystal to behave like a normal cubic dielectric, which is also known as the paraelectric state. The temperature at which the paraelectric-to-ferroelectric transition occurs is referred to as the Curie temperature (T_C), also known as the transition temperature or Curie point. In the high-temperature paraelectric state, the dielectric permittivity of the ferroelectric material follows the Curie-Weiss law, which is given as [16, 18]

$$\varepsilon' = \frac{C}{T - T_{CW}} \tag{1.6}$$

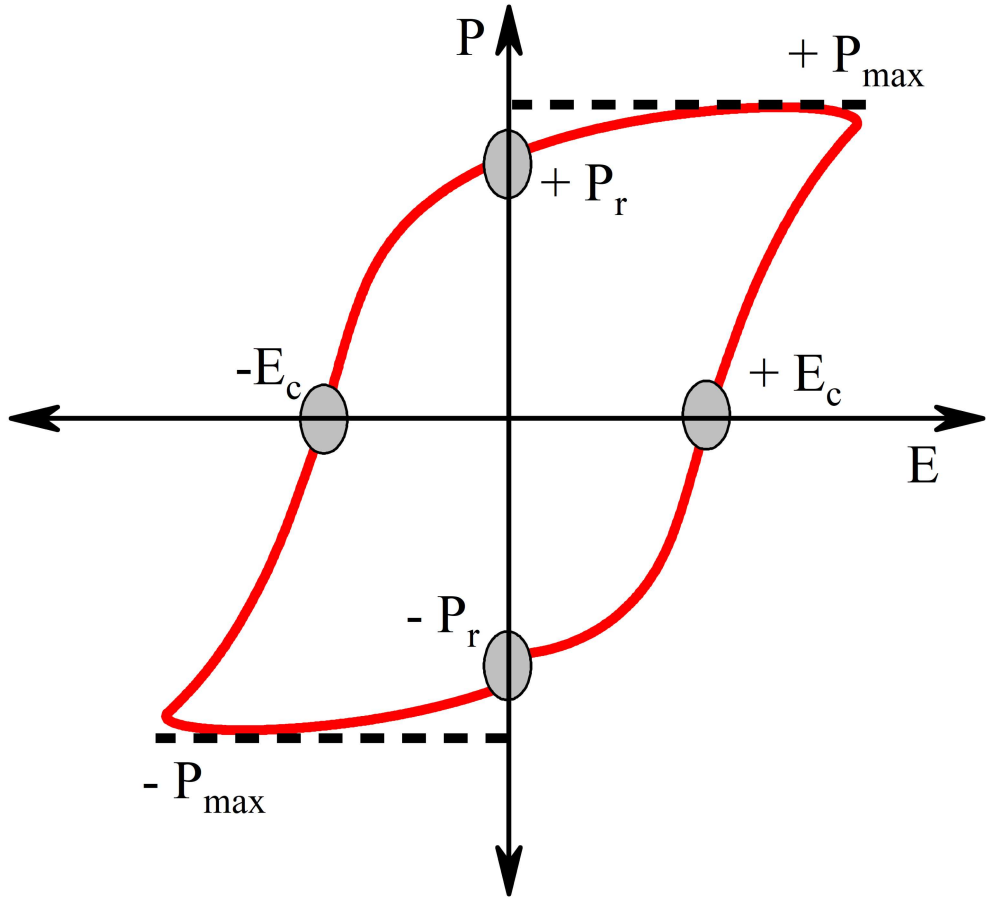

Fig. 1.4 Polarization *vs.* electric field (PE) hysteresis loop for a normal ferroelectric, having the remnant polarization (P_r) and coercive field (E_c).

where C is the Curie constant, T_{CW} is the Curie-Weiss temperature, and T is the temperature. It is important to note that in a second-order phase transition, the Curie-Weiss temperature (T_{CW}) is identical to the Curie temperature (T_C). However, for a first-order phase transition, these temperatures differ from each other.

The phenomenon of ferroelectricity, pyroelectricity, and piezoelectricity is closely related to the crystallographic symmetry of the material. We can understand this phenomenon on the basis of point group symmetry. There are seven crystal systems (cubic, tetragonal, hexagonal, rhombohedral, orthorhombic, monoclinic, and triclinic), and thirty-two point groups exist in three dimensions. Out of these 21 points groups (*1, 2, 3, 4, 6, m, mm2,*

3m, 4mm, 6mm, 222, 32, 422, 622, 23, 432, $\bar{4}, \bar{4}2m, \bar{6}, \bar{6}m2, \bar{4}3m$) are noncentrosymmetric [17]. Except for point group *432*, all the other 20 point groups exhibit piezoelectricity. Moreover, among the 20 piezoelectric point groups, ten point groups (*1, 2, 3, 4, 6, m, mm2, 3m, 4mm, and 6mm*) are inherently polar and possess pyroelectric properties. Among these ten point groups, those that demonstrate a reversal of polarization when subjected to an external electric field are known as ferroelectrics [9, 17]. Among ferroelectric materials, perovskite-based ferroelectrics are considered highly significant for both fundamental scientific studies and technological advancements.

1.3 Perovskite structure

Perovskites are a class of material with a structure similar to the mineral Calcium Titanate ($CaTiO_3$) [52, 53]. Perovskites have a general formula ABX_3. Here, A is usually a larger cation, B is a smaller cation, and X is an anion. At present, thousands of compounds are known those adopt the perovskite structure. The majority of perovskites with technical applications are oxides with the general form ABO_3. Bridgmanite, a perovskite-structured mineral, is the most abundant material in the Earth's lower mantle, having a composition (Fe, Mg)SiO_3). This structure exists at depths ranging from approximately 660 to 2900 kilometres and remains stable only under high temperatures and pressures.

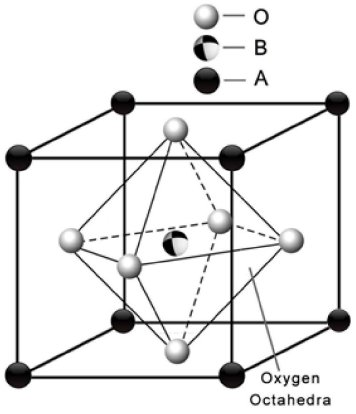

Fig. 1.5 The representation of the unit cell of an ideal cubic perovskite (ABO_3) structure.

To maintain the ionic neutrality of the perovskite oxides, we could have the following oxidation states of A and B cations

$$(q_A, q_B) = (+2, +4); \quad \text{for example, } BaTiO_3 \tag{1.7}$$

$$(q_A, q_B) = (+1, +5); \quad \text{for example, } NaNbO_3 \tag{1.8}$$

$$(q_A, q_B) = (+3, +3); \quad \text{for example, } BiFeO_3 \tag{1.9}$$

Here, q_A and q_B are the charges on the A and B site cations. Perovskite oxides exhibit remarkable tunability due to their flexibility of accommodating a wide variety of atoms at A and B sites. Moreover, they demonstrate a wide range of intriguing properties, including ferroelectricity, piezoelectricity, ferromagnetism, colossal magnetoresistance, electrocaloric effect, etc. [5, 54]. Barium Titanate ($BaTiO_3$) was the first polycrystalline ferroelectric material with a perovskite structure, which was discovered around 1944 [55]. This material was adopted in electronic applications, particularly in capacitors and transducers. Moreover, soon after the discovery of $BaTiO_3$ (BT), a lead-based system, $Pb(Zr,Ti)O_3$ (PZT), was discovered with superior piezoelectric properties and a higher Curie temperature (T_C) [56, 57]. This development reduced the interest in BT for piezoelectric applications. However, the adverse effects of lead on human health demands the development of lead-free functional materials.

1.3.1 The Goldschmidt tolerance factor

Apart from the good performance observed in perovskite-based materials, the stability of new functional materials remains a major issue [9]. Materials with ABO_3 composition can adapt different crystal structures depending on the cationic size/oxidation-state and interaction of the A-site cation with the corner-sharing BO_6 octahedra [58, 59]. The Goldschmidt tolerance factor (t) serves as an important empirical parameter for predicting

the stability of perovskite-structure [60, 61]. An ideal perovskite structure remains stable in a cubic structure with a lattice parameter (say a) [62, 63]. In this structure, the larger A cations occupy the corners of the cube, the B cation sits at the centre of the cube, and the O anions occupy the centre of the faces. From Fig. 1.5, it can be deduced that

$$\sqrt{2}a = 2R_{\mathrm{A}} + 2R_{\mathrm{O}}$$

$$a = \frac{2R_{\mathrm{A}} + 2R_{\mathrm{O}}}{\sqrt{2}} \tag{1.10}$$

and

$$a = 2R_{\mathrm{B}} + 2R_{\mathrm{O}} \tag{1.11}$$

Equating equations (1.10) and (1.11), we get:

$$\frac{2R_{\mathrm{A}} + 2R_{\mathrm{B}}}{\sqrt{2}} = 2R_{\mathrm{B}} + 2R_{\mathrm{O}} \tag{1.12}$$

$$1 = \frac{R_{\mathrm{A}} + R_{\mathrm{O}}}{\sqrt{2}(R_{\mathrm{B}} + R_{\mathrm{O}})} = \mathbf{t} \tag{1.13}$$

where t is called the tolerance factor, R_{A}, R_{B}, and R_{O} are the ionic radii of A, B, and O ions, respectively. Note that it is necessary to use ionic radii appropriate to the coordination geometry of the ions, i.e., ionic radii R_{A} and R_{B} should correspond to 12 and 6 coordination numbers, respectively. As shown above, the tolerance factor(t) for the ideal perovskite structure is 1 [53]. However, the value of the tolerance factor can be between ≈ 0.78 and ≈ 1.05, depending on the size of A and B site cations [64, 65]. Moreover, based on the value of the tolerance factor, the perovskite structure shows various phases [62, 66]. If the tolerance factor of the perovskite structure is $t < 1$, i.e., the A-site cation is comparably smaller in size, leading to octahedral rotation in the system [67]. The first perovskite structure, $CaTiO_3$, is one such system that exhibits octahedral rotations and stabilizes in

the orthorhombic phase (space group: *Pbnm*) [52, 67]. On the other hand, perovskites with t > 1 have a larger A-site cation that elongates the B-O bond length, leading to a shift of the B-site cation from its ideal centrosymmetric position. This, in turn, results in the 'B site-driven' ferroelectricity in the materials, e.g., Barium Titanate ($BaTiO_3$) [67, 68].

1.4 Tilt crystallography in distorted perovskites

A very limited number of perovskite structures are stabilized in an ideal cubic phase at ambient conditions with a Goldschmidt tolerance factor of t = 1, such as $SrTiO_3$. However, the majority of naturally occurring perovskite structures are distorted [58]. Moreover, distortions are crucial in determining the physical properties and functionalities of materials. The structural distortions in perovskite-based systems can be broadly categorized into three main categories:

(i) Octahedral tilting.

(ii) Cationic displacement (parallel (ferroelectrics) or antiparallel (antiferroelectrics)).

(iii) Octahedral distortions.

Moreover, these distortions can occur independently or in combination with each other. For instance, $CaTiO_3$ primarily undergoes octahedral tilting, whereas $BaTiO_3$ exhibits B-site cationic displacements [67, 68]. In contrast, $NaNbO_3$ displays a combination of both octahedral tilting and cation displacements, resulting in complex structural and functional behaviour [69]. Moreover, if octahedral tilt is the primary order parameter, then it plays a crucial role in determining the space group symmetry of perovskites [58, 59]. It also influences various physical properties, *viz.,* dielectric, ferroelectric, and electromechanical responses, making it critical in the design and application of perovskite-based functional materials.

At very high temperatures, most of the perovskites adopt a high symmetry cubic structure with the $Pm\bar{3}m$ space group. However, as the temperature decreases, structural

distortions such as cation displacements and/or octahedral tilting set in, thereby resulting in low-symmetry distorted structures. The tilt systems (simple/compound) exhibited by the perovskite structures were first formulated by Glazer in his groundbreaking work, published in Acta. Cryst. [58, 59]. For small tilt angles (less than 15°), the pseudo-cubic axial lengths can be written in terms of the anion-anion distance through the center of the octahedron and tilt angles. In Glazer's notation (e.g., $a^-b^-c^-$), the magnitudes of the tilts are represented by a set of three letters *(a, b, c)* corresponding to [100], [010], and [001] directions. The equality of tilt angles is represented by repeating the corresponding letter. For example, a simple tilt system $a^-a^-c^+$ indicates that the magnitude of the tilting of two axes is equal (i.e., along [100] and [010]), and is different from the tilt of the third axis (i.e, [001]) [58, 59]. The manner in which two adjacent octahedra rotate relative to each other determines the tilt pattern. For instance, when adjacent octahedra tilt in the same direction, the tilting is referred to as in-phase (positive; +) tilt, whereas if they rotate in opposite directions, the tilting is referred to as out-of-phase (negative; -) tilt. On the other hand, the symbol "0" in the superscript represents the absence of tilting. Fig. 1.6 represents no tilt, out-of-phase tilt, and in-phase tilt in the perovskite structures [1]. Later on, Stokes et al. introduced a modified version of Glazer's notation to provide additional information regarding the displacement of ferroelectric cation along a particular axis using subscripts in conventional notation [63].

The presence of octahedral tilting influences the crystal structure in various ways, e.g., the unit cell dimensions get multiplied along one, two, or three crystallographic axes depending upon the tilt pattern. Moreover, the multipled unit cell axes is/are reflected by the appearance of weak reflections (known as superlattice reflections) in the diffraction patterns. There are two types of reflections in the diffraction patterns of perovskites: (i) main perovskite reflections (corresponding to the basic cell), and (ii) superlattice reflections (corresponding to multipled cell). These reflections can be indexed with respect

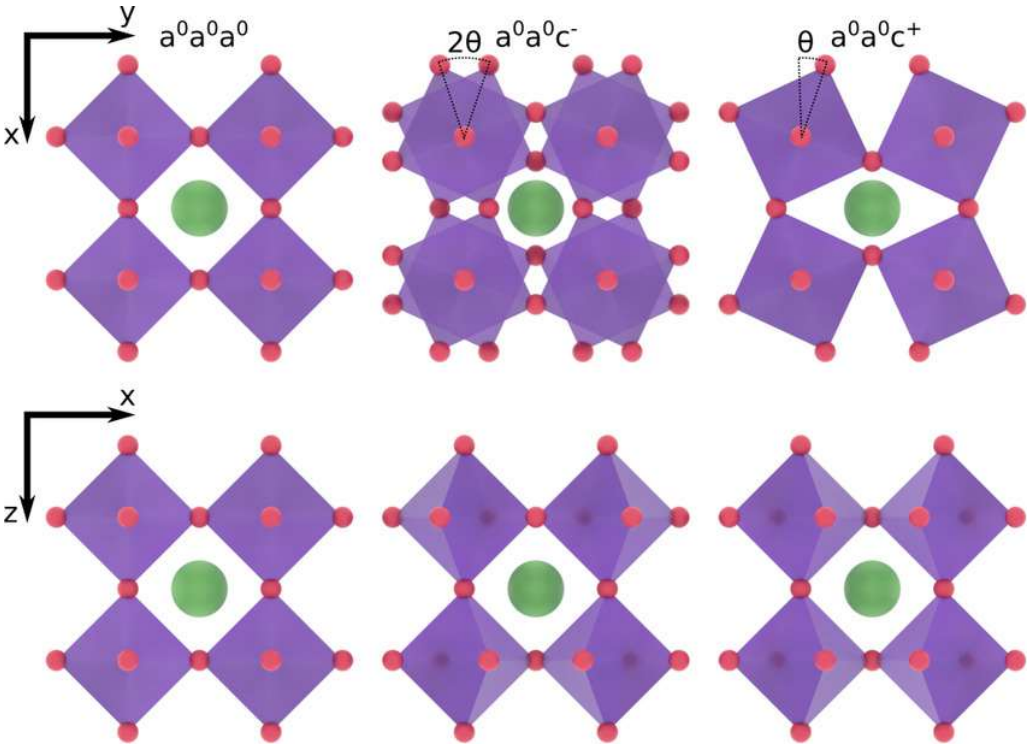

Fig. 1.6 Illustration of different octahedral tilting. The left column shows $a^0a^0a^0$ (no tilt), the middle column shows $a^0a^0c^-$ (out-of-phase tilting), and the right column shows $a^0a^0c^+$ (in-phase tilting). The upper (lower) row shows the structures in the xy-plane (zx-plane); adopted from [1].

to a doubled pseudocubic cell as per Glazer [59, 70]. Reflections with even-even-even (eee) type hkl indices correspond to main perovskite reflections, while reflections with odd-even-even (oee), odd-odd-even (ooe), and odd-odd-odd (ooo) indices correspond to antiparallel cationic displacements, in-phase octahedral rotations, and out-of-phase octahedral rotations, respectively [59, 70]. The out-of-phase and in-phase octahedral rotations result from the hardening of soft phonon modes corresponding to R (q = 1/2,1/2,1/2) and M (q = 1/2,1/2,0) points of the cubic Brillouin zone [58, 59, 71, 72].

Further, ferroelectric perovskites, such as Barium Titanate ($BaTiO_3$), demonstrate off-centering of the B-site cation (Ti^{+4}) within the oxygen octahedron, resulting in a non-zero polarization [67, 68]. This type of cationic displacement is responsible for the appearance of spontaneous polarization. [73]. In this case, no extra reflection (i.e.,

superlattice reflection) will appear in the diffraction pattern; rather, splitting of the main perovskite reflections will be observed. In contrast, antiferroelectric materials, such as Sodium Niobate ($NaNbO_3$), exhibit antiparallel ionic displacements, resulting in the zero net polarization [6, 36, 69].

1.5 Symmetry mode analysis of distorted structure

Low symmetry structures observed in perovskite oxides can be derived from high-symmetry cubic structure (with $Pm\bar{3}m$ space group) by incorporating symmetry allowed distortions. Further, these distortions result from static displacements offered by the condensation of soft phonon modes (referred to as frozen phonon modes) corresponding to the zone centre and (or) zone boundary of the cubic Brillouin zone [74]. Structural distortion(s) in perovskites are quantified by the amplitude of various frozen phonon mode(s), whose symmetry is given by an irreducible representation(s) of the high symmetry (parent) space group. The mode(s) driving the phase transition are considered primary and have high amplitudes. Other symmetry allowed modes having small amplitudes are considered secondary [72]. The amplitude of the frozen phonon mode may vary as a function of external stimuli such as temperature, pressure, composition, etc., and can be treated as an order parameter to describe structural phase transitions [72, 74, 75, 76]. Now, if the high symmetry parent structure corresponds to Group G and the low symmetry distorted structure corresponds to group H, such that H is a subgroup of G, then symmetry breaking equation can be expressed as

$$r(\mu,i) = \mathbf{r}_0(\mu,i) + \mathbf{u}(\mu,i) \tag{1.14}$$

where $r(\mu,i)$ and $\mathbf{r}_0(\mu,i)$ are the positions of atoms in the low and high symmetry structures and $\mathbf{u}(\mu,i)$ represents the atomic displacements in the asymmetric unit of the

low symmetry structure. Here, μ (1,.....n) and i represent the type of atoms and Wyckoff site splitting of the parent structure. By using the symmetry mode analysis, we can break static displacements of the atoms in terms of various frozen phonon modes [74, 75]. It is important to note that the total number of refinable atomic coordinates is equal to the number of allowed modes. The magnitude of distortion in the displacive phase transition is determined by the amplitude of symmetry-adapted modes. In general, any structural distortion can be represented as the sum of symmetry-adapted modes. Below are the two examples in which we have employed symmetry mode analysis to explore the structural phase transitions.

1.6 Symmetry-mode analysis examples

1.6.1 Symmetry mode analysis of $EuNiO_3$

An intriguing example to investigate the co-operative phenomenon between the electronic, magnetic, and lattice degrees of freedom could be found in the series of perovskite structured rare earth nickelates ($RNiO_3$), where R is any rare earth ranging from Lutetium (Lu) to Lanthanum (La) [77, 78]. All members of the series (except $LaNiO_3$) exhibit a sharp metal-to-insulator phase transition on decreasing temperature. This transition is accompanied by a symmetry-lowering from high-temperature metallic phase (orthorhombic *Pbnm*) to low-temperature insulating phase (monoclinic $P2_1/n$) with a significant change in conductivity at M-I transition temperature (T_{M-I}) [79]. In Metallic region, conduction takes place due to overlapping of p and d orbitals corresponding to oxygen and nickel, respectively, and the *charge transfer mechanism* is given by $d_i^{3+}p_j^{2-} \leftrightarrow d_i^{2+}p_j^{1-}$ [78]. Just below T_{M-I}, nickelates behave as charge transfer semiconductors. This insulating phase is known to have two non-equivalent Ni sites with slightly different averaged Ni-O bond lengths. This subtle Ni site splitting below T_{M-I} results in a charge-ordered system, and the

charge disproportion among the two Ni sites is given by $2Ni^{3+} \rightarrow Ni^{3+\delta} + Ni^{3-\delta}$ [80, 81]. In addition, all rare-earth nickelates order antiferromagnetically below Neel temperature (T_N), which is the same as T_{M-I} for Pr and Nd and lower than T_{M-I} for smaller cations [81]. $EuNiO_3$, a member of $RNiO_3$ series, exhibits three distinct phases resulting from two phase transitions, *viz.,* paramagnetic metal $\rightarrow$ paramagnetic insulator (M-I) and paramagnetic insulator $\rightarrow$ antiferromagnetic insulator(Neel temperature) occuring at $T_{M-I} \approx 460K$ and $T_N \approx 200K$, respectively [82] [78, 83]. The evidence of two non-equivalent Ni sites in the insulating phase has been verified earlier with the aid of Mössbauer spectroscopy [84] and X-ray photoemission spectroscopy [85]. However, it has been reported that a single orthorhombic *Pbnm* ((tilt system: $a_0^- a_0^- c_0^+$; cell size: $\sqrt{2}a_p \times \sqrt{2}b_p \times 2c_p$)) phase is stable for the analysed temperature range [86]. In our study, we have reinvestigated Metal-Insulator and Neel transition using symmetry mode analysis. For this purpose, we have reused the Synchrotron X-ray diffraction data from a study on $EuNiO_3$ published in Dalton transaction(RSC) by Federico et al. [86]. The orthorhombic *Pbnm* phase of $EuNiO_3$ has been described by the superposition of various symmetry-adapted modes corresponding to an ideal cubic structure [87]. For quantifying the symmetry-adapted modes, we have used AMPLIMODES, a program available at Bilbao crystallography server [74, 75]. As an input for AMPLIMODES, we have used the primitive cubic cell (space group: $Pm\bar{3}m$) and orthorhombic cell (space group: *Pbnm*) as high and low symmetry structures, respectively [88]. Eu, Ni, and O atoms occupy 1b (0.5,0.5,0.5), 1a (0,0,0), and 3d (0.5,0,0) Wyckoff sites respectively, in a high symmetry cubic phase of $EuNiO_3$. The transition from cubic phase to orthorhombic phase occurs via splitting of the Wyckoff site in the fashion given in Table 1.1. The static displacement resulting from the synergistic coupling of the two primary modes, *viz.,* R_4^+ and M_3^+ leads to a symmetry breaking transition: $Pm\bar{3}m \rightarrow Pbnm$. These two primary order parameters are linked with R (q = 1/2,1/2,1/2) and M (q = 1/2,1/2,0) points of the cubic Brillouin zone and result in out-of-phase and in-phase rotation of the octahedra

Table 1.1 Wyckoff sites occupied by atoms in low- and high-symmetry structures, along with phonon modes responsible for symmetry breaking.

Wyckoff site splitting		
space group: *Pm$\bar{3}$m*	**Symmetry breaking modes**	**space group: *Pbnm***
Eu **1a**	X_5^+(Eu), R_5^+(Eu)	Eu **4c**
Ni **1b**	-	Ni **4b**
O **3d**	R_4^+, M_3^+, X_5^+(O), R_5^+(O), M_2^+	O1 **4c**, O2 **8d**

[63, 89, 90, 91]. Two other secondary modes with considerably high amplitudes, *viz.,* $X_5^+(q = 0, 1/2, 0)$ and $R_5^+(q = 1/2, 1/2, 1/2)$ contribute effectively to the displacement of A site cation. Fig. 1.7 depicts the schematic representation of the seven distortion modes involved in the orthorhombic *Pbnm* phase. For clear representation, different figures have been used to show the displacement patterns of modes involving more than one atom, for example, Fig. 1.7 (a) & (b) for R_5^+ (corresponding to O and Eu atoms) and Fig. 1.7 (c) & (d) for X_5^+ (corresponding to O and Eu atoms). In Fig. 1.8, we have plotted amplitude of $R_5^+(Eu)$ and $X_5^+(Eu)$ modes as a function of temperature. The amplitudes of these phonon modes increase with decrease in temperature, suggesting an enhancement in distortion at low temperatures. Further, the anomalies in amplitudes of modes at $T_{M\text{-}I} \approx 463$ K and $T_N \approx 200$ K, corroborate the two phase transitions *viz.,* Metal-Insulator and paramagnetic $\rightarrow$ antiferromagnetic (Neel) transitions. These two modes are of particular importance in our case since we are using synchrotron X-rays to probe the crystal structure, which is more susceptible to heavier atoms due to their high electron density. Hence, X-rays can be used to capture the subtle displacement of heavy Eu atoms. Furthermore, the Neutron diffraction experiment is not feasible in the case of $EuNiO_3$ due to highly absorbing nature of Eu atoms.

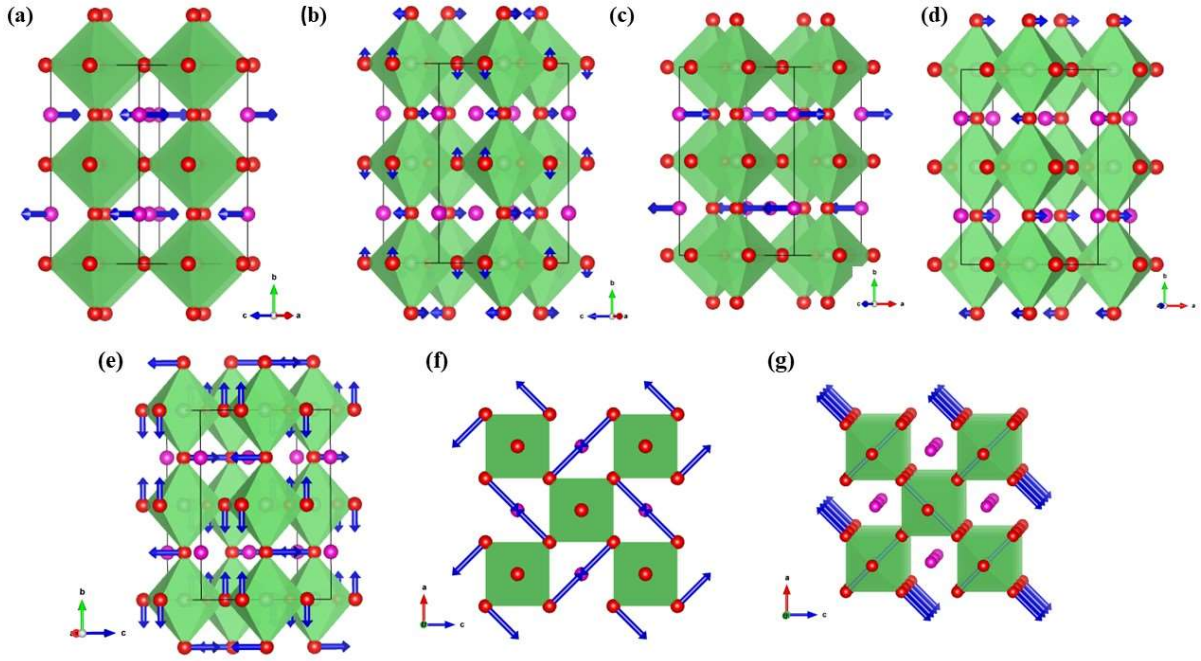

Fig. 1.7 Schematic representation of the atomic displacement pattern of various distortion modes involved in the symmetry-breaking transition $Pm\bar{3}m \rightarrow Pbnm$: (a) R_5^+(Eu), (b) R_5^+(O), (c) X_5^+(Eu), (d) X_5^+(O), (e) R_4^+, (f) M_3^+, (g) M_2^+. Irreducible representations affecting more than one atom (X_5^+ and R_5^+) are represented separately.

1.6.2 Symmetry mode analysis of $RFeO_3$ (R=Lanthanide)

Rare earth orthoferrites are a class of magnetic materials having a chemical configuration $RFeO_3$ where Rare earth (R) and Iron (Fe) cations occupy A and B sites of ABO_3 structure [92, 93, 94, 95]. The room temperature structure of $RFeO_3$ is orthorhombic *Pbnm* with $a_0^- a_0^- c_0^+$ tilt system (Cell size: $\sqrt{2}a_p \times \sqrt{2}b_p \times 2c_p$) in modified Glazer's notation, where a_p, b_p, and c_p are lattice parameters of basic cell [58, 59]. The crystal structure of these materials consists of two types of magnetic sublattices: one corresponding to the rare earth cations and the other to iron cations. At high temperatures, the R and Fe sublattices are disordered, and the material exhibits a paramagnetic nature. However, as the temperature is lowered, the iron sublattice in $RFeO_3$ orders antiferromagnetically below Neel's temperature that ranges between 620-740 K depending upon the ionic radii of rare earth [96, 97, 98]. The antiferromagnetic sublattice of Fe cations is slightly canted,

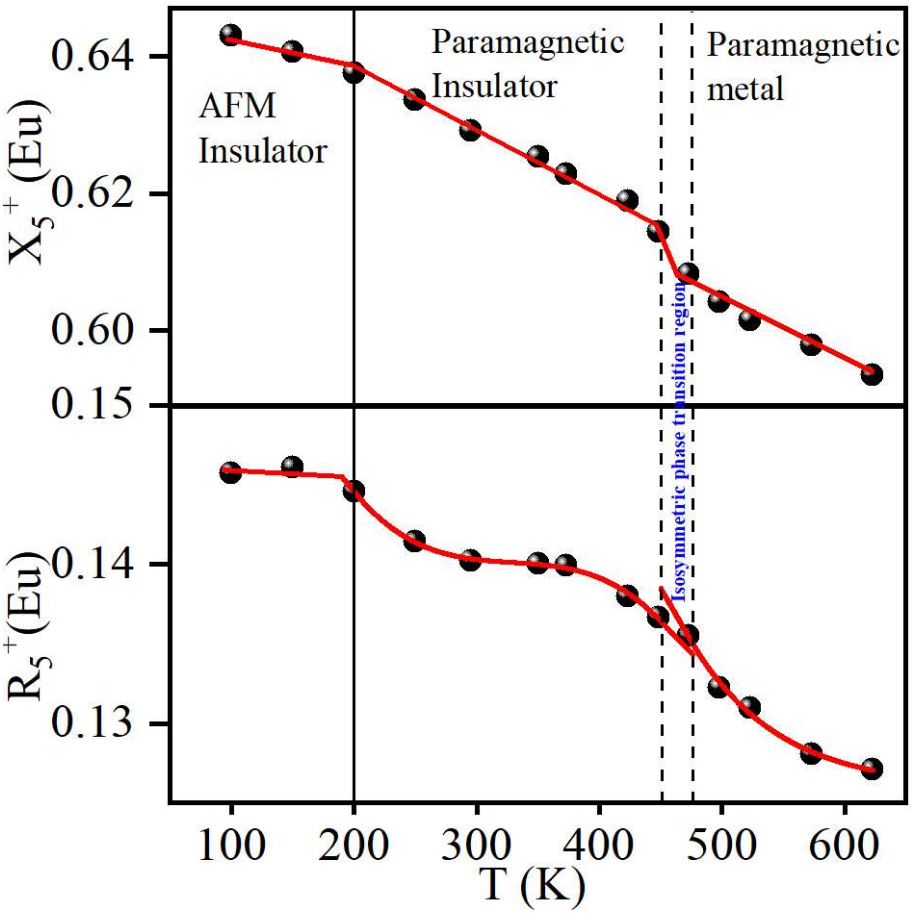

Fig. 1.8 Temperature-dependent evolution of X_5^+(Eu) and R_5^+(Eu) phonon mode amplitudes. These two modes are responsible for the displacement of the Eu atom from its position in an ideal cubic structure.

which gives a small ferromagnetic component [99]. On the other hand, the ferromagnetic ordering of R cations occurs at cryogenic temperatures (i.e., below 10 K) [97]. The ordering and interaction of A and/or B sublattices may lead to various exotic phenomena such as magnetization reversal, spin reorientation, magnetoelectric coupling, multiferroicity, etc. [93, 98, 100, 101, 102, 103]. Although the crystal structure remains orthorhombic with *Pbnm* space group for all rare-earth ferrites, yet anomalous changes in lattice parameters have been observed as a function of rare-earth cationic radii, suggesting an isosymmetric phase transition (ISPT) [92]. To explore this ISPT, we did symmetry mode analysis using the crystallographic information available in literature [92, 104].

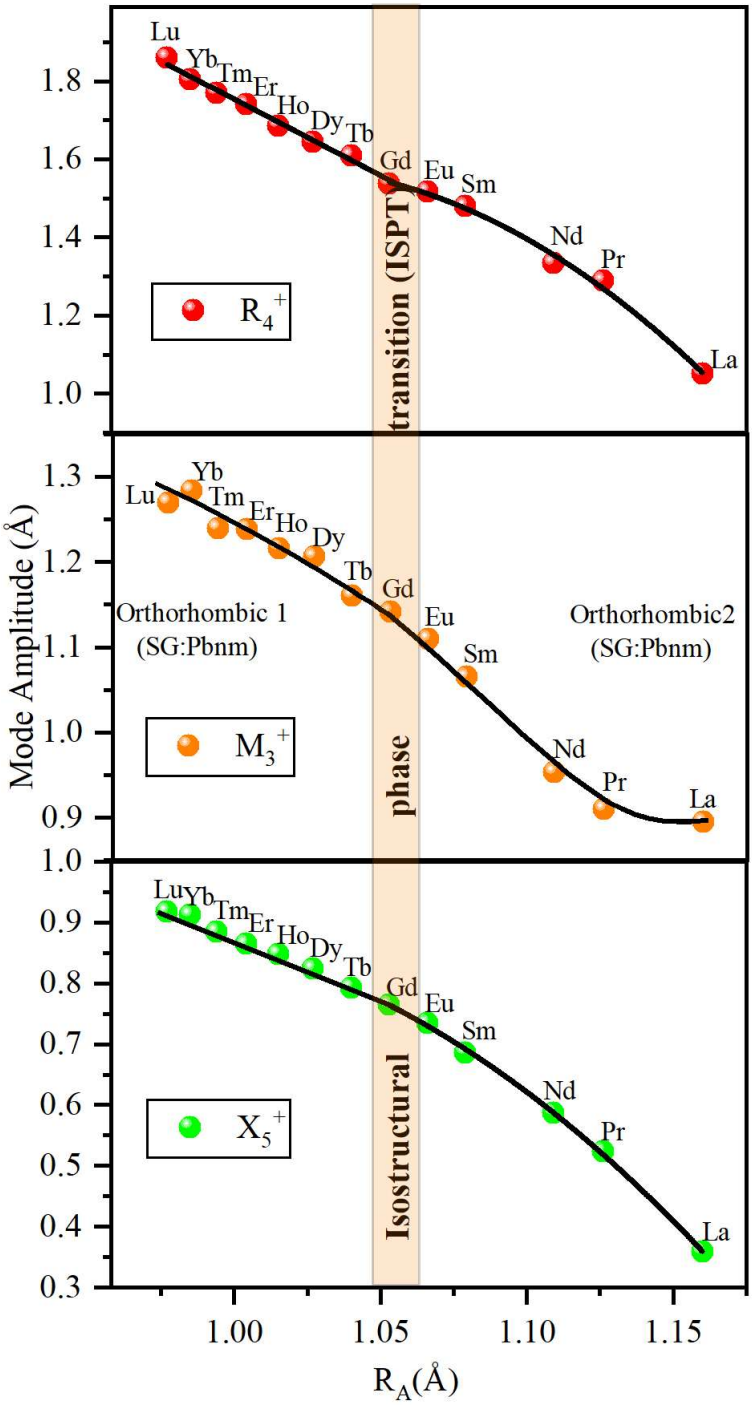

Fig. 1.9 Evolution of amplitude of various phonon modes as a function of R cationic radii.

Table 1.2 Space Group of $RFeO_3$ compounds with corresponding references.

$RFeO_3$ Structure	Space Group	Reference
$LaFeO_3$	$Pbnm$	[104]
$PrFeO_3$	$Pbnm$	[92]
$NdFeO_3$	$Pbnm$	[92]
$SmFeO_3$	$Pbnm$	[92]
$EuFeO_3$	$Pbnm$	[92]
$GdFeO_3$	$Pbnm$	[92]
$TbFeO_3$	$Pbnm$	[92]
$DyFeO_3$	$Pbnm$	[92]
$HoFeO_3$	$Pbnm$	[92]
$ErFeO_3$	$Pbnm$	[92]
$TmFeO_3$	$Pbnm$	[92]
$YbFeO_3$	$Pbnm$	[92]
$LuFeO_3$	$Pbnm$	[92]

The crystallographic information files (CIFs) were obtained from the crystallographic open database and are listed below in Table 1.2. To calculate the amplitude of various symmetry adapted modes involved in the symmetry-breaking transition, we have performed symmetry mode analysis for $RFeO_3$ using AMPLIMODES available at the Bilbao crystallographic server [74, 75]. A common parent structure with cubic space group $Pm\bar{3}m$ has been used with A atom at 1b (0.5, 0.5, 0.5); B atom at 1a (0, 0, 0), and O atom at 3d (0.5, 0, 0) sites, respectively. The transformation matrix relating high ($Pm\bar{3}m$) and low ($Pbnm$) symmetry structures is

$$\begin{bmatrix} 1 & 1 & 0 \\ -1 & 1 & 0 \\ 0 & 0 & 2 \end{bmatrix} \begin{bmatrix} 1/2 \\ 1/2 \\ 0 \end{bmatrix} \tag{1.15}$$

In an orthorhombic structure with $Pbnm$ space group, there are distortions corresponding to seven modes with five unique irreps of the parent space group $Pm\bar{3}m$. Considering pure displacive nature, the symmetry lowering occurs as follows:

(i) R cation: Wyckoff site 1b of $Pm\bar{3}m$ transforms into 4c site of $Pbnm$ via $R_5^+(q =$

$1/2,1/2,1/2)$ and $X_5^+(q=0,1/2,0)$ modes.

(ii) Fe cation: Wyckoff site 1a of $Pm\bar{3}m$ transforms into 4b site of *Pbnm*.

(iii) O atom: Wyckoff site 3d of $Pm\bar{3}m$ splits into 4c and 8d sites of Pbnm via five modes *viz.*, $R_4^+(q=1/2,1/2,0)$, $M_3^+(q=1/2,1/2,0)$, $M_2^+(q=1/2,1/2,0)$, $R_5^+(q=1/2,1/2,1/2)$, and $X_5^+(q=0,1/2,0)$.

As discussed earlier, the structural distortion present in the low-symmetry structure contains a primary component that corresponds to mode(s) that are unstable in the parent structure and are fundamental for explaining the stability of the distorted structure [74, 75]. It is important to note that the coupling between R_4^+ and M_3^+ modes drives the symmetry-breaking phase transition *viz.*, $Pm\bar{3}m \rightarrow Pbnm$. Hence, these two modes act as the primary order parameters for this transition. All the other modes *viz.*, $X_5^+(q=0,1/2,0)$, $R_5^+(q=1/2,1/2,1/2)$, $M_2^+(q=1/2,1/2,0)$ are secondary modes and become energetically favourable in the presence of primary modes. In Fig. 1.9, we have plotted the variation of the amplitude of primary modes *viz.*, $R_4^+(q=1/2,1/2,1/2)$ and $M_3^+(q=1/2,1/2,0)$ which have significantly high amplitude. In addition, we have also plotted the amplitude of the X_5^+ mode since it has an amplitude comparable to the primary modes and is related to the displacement of the A-site cation which drives the isosymmetric phase transition (ISPT) [72]. The anomalous changes in the amplitudes of various phonon modes around Gd authenticate our idea of ISPT. Thus, unexplored signatures of ISPT were revealed in $RFeO_3$ using the mode crystallographic approach for the very first time.

1.7 Phase boundary engineering in perovskite-based solid-solutions

The enhancement in the dielectric and piezoelectric properties of functional materials arises from two distinct contributions, commonly referred to as extrinsic and intrinsic sources [105, 106, 107, 108]. Extrinsic factors contributing to the enhancement of functional properties include grain size, domain size, domain wall mobility, preferred orientation, etc. [9]. On the other hand, the intrinsic contribution arises from lattice distortions and is directly linked with the changes in the unit cell polarization [105]. Generally, the large electromechanical response of the functional materials arises from polarization extension and polarization rotation phenomenon [30]. Here, the polarization rotation refers to the continuous reorientation of the electric dipole moment (spontaneous polarization) within the crystalline lattice under the influence of an external electric field. Whereas the polarization extension refers to the increase in the magnitude of the spontaneous polarization of the crystal under an external electric field. It is important to note that the polarization rotation is most pronounced in regions where multiple ferroelectric phases with distinct polarization directions coexist, typically occur-

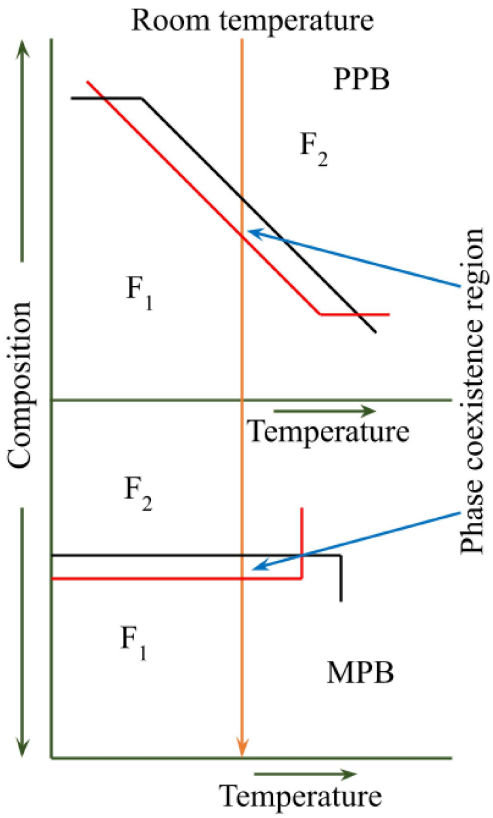

Fig. 1.10 Schematic representation of polymorphic phase boundary (PPB) and morphotropic phase boundary (MPB) existing between two ferroelectric phases, F_1 and F_2.

ring during ferroelectric–ferroelectric (FE–FE) phase transitions, whereas polarization extension is associated with paraelectric–ferroelectric (PE–FE) phase transitions [30, 109]. There are two different phase boundaries which have been widely exploited for technological applications: (i) Morphotropic Phase Boundary (MPB), (ii) Polymorphic Phase Boundary (PPB). A phase boundary indicating a composition-induced transition between different ferroelectric phases is known as a Morphotropic Phase Boundary (MPB) [29]. In contrast, a temperature-induced transition between ferroelectric phases is referred to as a Polymorphic Phase Boundary (PPB) [29]. While the mechanisms responsible (polarization rotation/extension) for the enhancement of physical properties are similar for both types of phase boundaries, they differ in terms of their thermal stability [9, 29]. The MPBs are nearly temperature independent (weakly temperature dependent) while PPBs are highly temperature sensitive (see Fig. 1.10). Later, it was found that the high piezoelectric response near MPBs can be attributed to flattening of the free-energy profile as a function of composition [110].

The idea of Morphotrpoic/Polymorphic phase boundary for enhancing physical properties has been extensively exploited in various lead-based and lead-free compositions such as $Pb(Ti_xZr_{1-x})O_3$, $Pb(Mg_{1/3}Nb_{2/3})O_3$–$PbTiO_3$, $Pb(Zn_{1/3}Nb_{2/3})O_3$–$PbTiO_3$, $Li_{0.8}Na_{0.2}NbO_3$, $K_{0.5}Na_{0.5}NbO_3$ and so on [28, 56, 90, 111, 112, 113, 114]. The Morphotropic phase boundary in $Pb(Ti_xZr_{1-x})O_3$ (PZT) is stable within the composition range $0.48 \leq x \leq 0.50$, separating the Zr-rich rhombohedral phase from the Ti-rich Tetragonal phase [28, 56]. Thus, MPB in PZT can be considered as a phase boundary between rhombohedral (space group: *R3m*) and tetragonal (space group: *P4mm*) phases (see Fig. 1.11). Later, it was discovered that a monoclinic phase acts as a bridge between the two ferroelectric phases. Multiple research groups have identified several monoclinic phases in MPB-based systems, namely M_A, M_B, and M_C, which correspond to the *Cm*, *Cm*, and *Pm* space groups, respectively [21, 56, 115, 116, 117]. Although these bridging phases share the same sym-

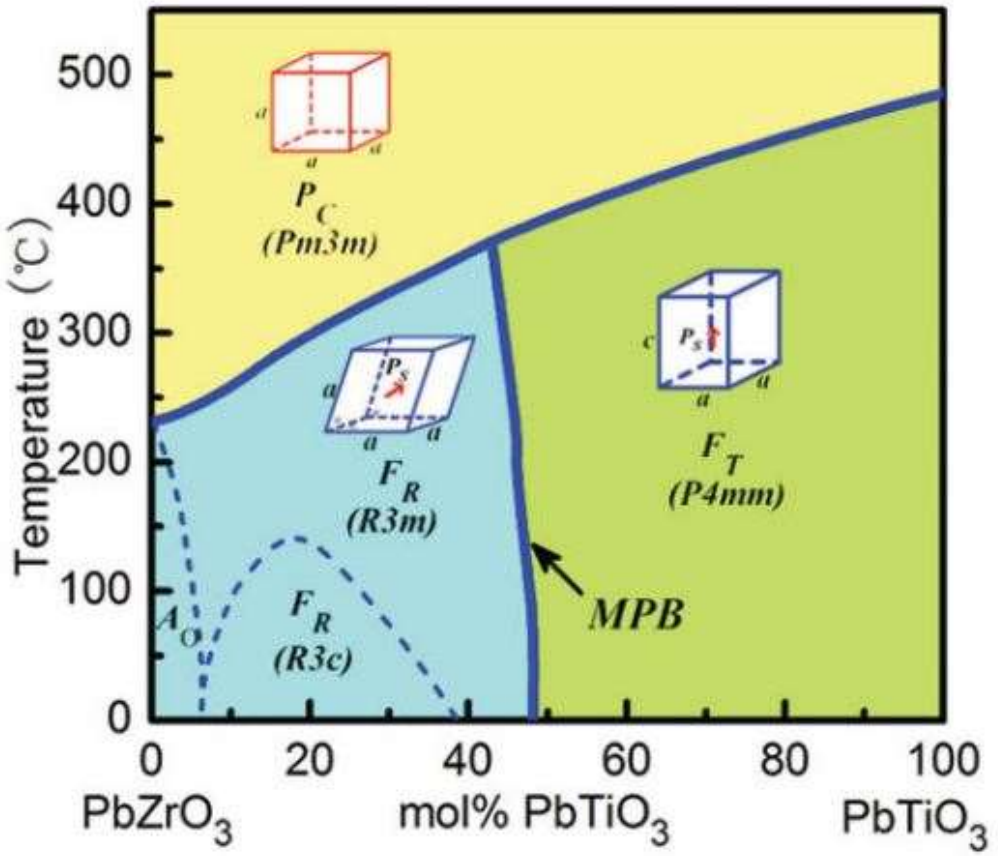

Fig. 1.11 Morphotropic phase boundary in $Pb(Zr,Ti)O_3$ [2]

metry (i.e., monoclinic), they are distinguished by differences in their polarization vectors (see Fig. 1.12). As previously mentioned, polymorphic phase boundaries (PPBs) exhibit strong temperature dependence, unlike morphotropic phase boundaries (MPBs), which are relatively insensitive to temperature changes, making PPBs less favourable for commercial applications. To address this limitation, the present thesis explores the concept of PPBs exhibiting tilt-oriented ferroelectric phases, since octahedral tilts provide excellent thermal stability to perovskite-based systems [118, 119].

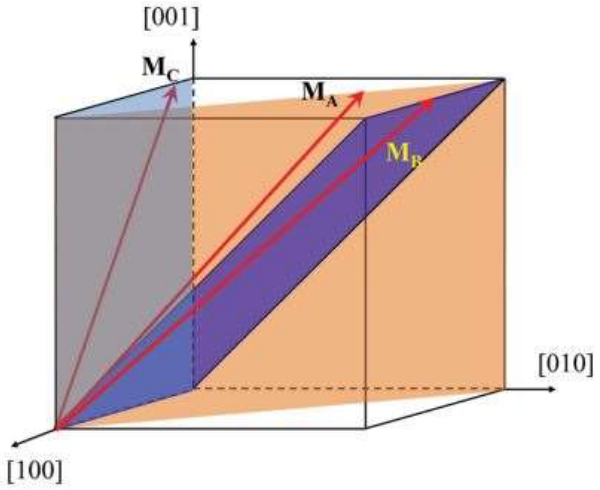

Fig. 1.12 Schematic representation of polar directions in monoclinic M_A, M_B, and M_C phases [3].

1.8 Relaxor ferroelectrics

Relaxor ferroelectrics (or Relaxors) have attracted continued interest due to their unusual properties, such as giant dielectric permittivity, electrostriction, etc. [120, 121, 122]. Relaxors were first discovered by Smolenskii and co-workers in 1958 [123]. Unlike normal ferroelectrics, relaxors demonstrate the following characteristics : (a) The temperature-dependent dielectric permittivity exhibits a broad maximum (see Fig. 1.13), (b) The maxima of the dielectric permittivity are frequency-dependent, and (c) They do not undergo a long-range phase transition below the dielectric maxima [120, 124, 125]. Large dielectric permittivity observed in a broad temperature range, accompanied by high electrostrictive coefficients and an almost hysteresis-free strain, have made relaxors a material of choice for high-end industrial applications [126, 127].

The unique properties of relaxors are associated with nano-sized polar regions (known as Polar nano regions) embedded in a non-polar matrix and their temperature-dependent dynamics (see Fig. 1.14). The schematic evolution of Polar nano regions (PNRs) as a function of temperature is shown in Fig. 1.15. Below Burns temperature (T_B), which is typically few hundred degrees above T_m (i.e., temperature corresponding to dielectric

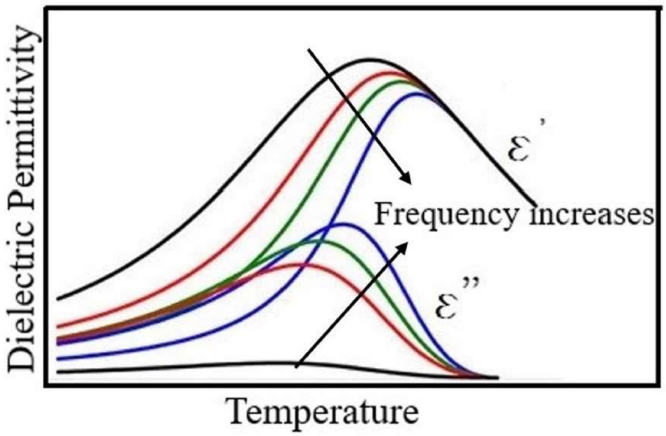

Fig. 1.13 Schematic representation of dielectric permittivity behaviour exhibited by relaxor ferroelectrics [4].

maximum), PNRs begin to nucleate, and their size/volume progressively increases on decreasing temperatures [128, 129]. Just below T_B, the PNRs remain highly uncorrelated, leading to a zero time-averaged polarization. The presence of PNRs can be inferred from properties such as the temperature dependence of refractive index, Raman spectroscopy, and the thermal expansion coefficient [130, 131]. On cooling below T_B, an intermediate temperature T^* is observed, where PNRs begin to interact and transit into a static state from a dynamic state [132, 133, 134]. On further cooling, the PNRs become completely static and form a glass-like structure below a temperature known as Vogel-Fulcher freezing temperature T_{VF} [130]. Unlike conventional ferroelectrics, most of the relaxors do not exhibit a long-range ferroelectric ordering at low temperature [135]. However, for canonical relaxors, a long-range ferroelectric ordering can be stabilized at low temperatures (below T_{VF}) on the application of a suitable external electric field [136]. Interestingly, there are relaxors demonstrating a long-range ferroelectrically ordered state below T_{VF} even in the absence of an electric field [137, 138, 139, 140, 141]. Relaxors can be divided into two major categories based on the behaviour demonstrated by them below T_{VF}. The first category includes relaxors exhibiting a long-range ferroelectric order below T_{VF} (e.g. $PbMg_{1/3}Nb_{2/3}O_3$-x $PbTiO_3$ (PMN-PT))[140] while the second category do not experience

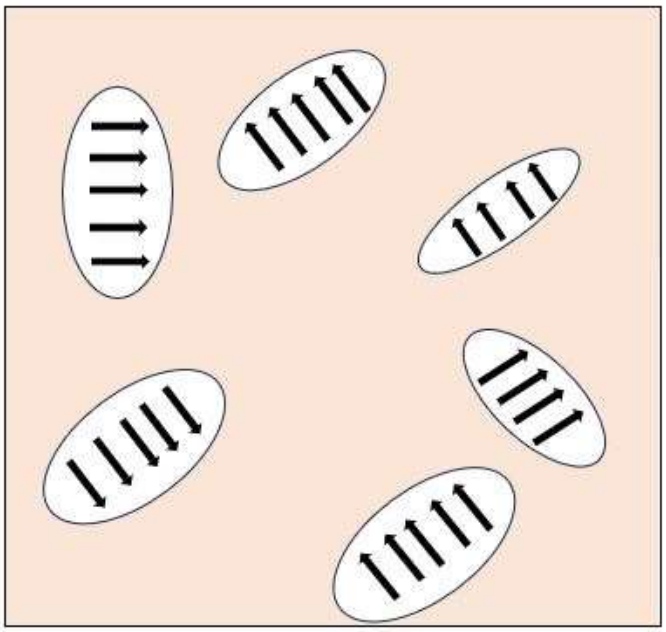

Fig. 1.14 Polar nano regions in a non-polar matrix.

a phase transition even at the cryogenic temperatures and demonstrates an average cubic structure throughout (e.g. $PbMg_{1/3}Nb_{2/3}O_3$ (PMN)) [142, 143].

The dynamics of PNRs as a function of temperature are not yet well understood, and it remains an important topic in condensed matter physics [120, 125, 144, 145]. Numerous models have been proposed to explain the characteristics of relaxors, some of which are discussed below. Smolensky et al. were the first to explain the relaxor behaviour using a model based on chemical heterogeneity [146]. They observed that the dielectric permittivity of relaxors could not be explained by first-order or second-order phase transitions. They suggested that the diffuseness in dielectric permittivity arises from compositional fluctuations due to the presence of different cations occupying the same crystallographic site, e.g., $PbMg_{1/3}Nb_{2/3}O_3$ (PMN). Furthermore, the frequency dependence of the dielectric maxima arises from the movement of boundaries between various polar (chemically ordered) regions (having a size distribution) in a non-polar matrix [146]. The curie point of these polar regions depends on their size, and they

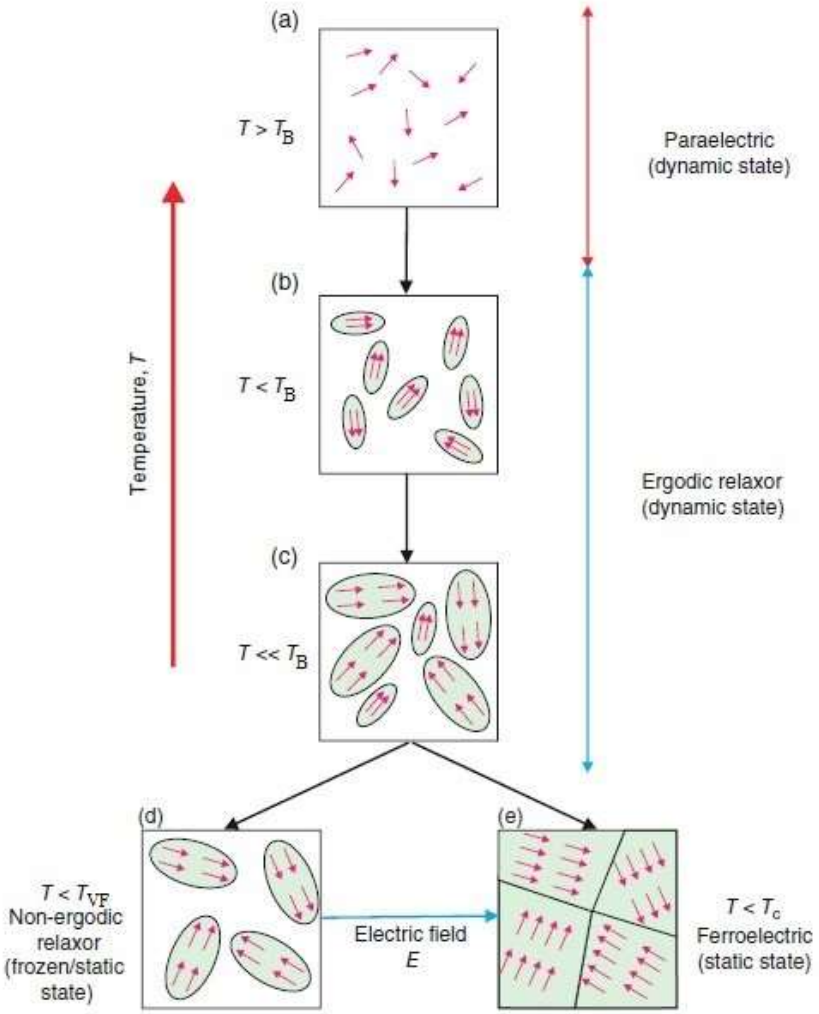

Fig. 1.15 Schematic representation of polar nano-regions in the cubic matrix [5].

collectively form a statistical distribution [146]. Later, Cross et al. questioned the concept of local Curie points and proposed the super paraelectric model for relaxors while still acknowledging the role of chemical heterogeneity [147]. They argued that for very small polar regions, the energy barrier for polarization switching becomes comparable to thermal energy. Further, they referred this state as a superparaelectric in which thermal energy neutralizes the existing polarity, in close analogy to superparamagnetism. They showed that while polarization values diminish rapidly at temperatures above T_m, a significant RMS polarization remains even above T_m. This suggests that at temperatures above T_m,

PNRs remain highly dynamic, with their polarization vectors continuously flipping among energetically equivalent directions. The core idea of the superparaelectric model is that the local (polar) symmetry is lower than the global (non-polar) symmetry. However, this model could not explain frequency dispersion in the dielectric permittivity. Moreover, Cross et al. predicted that a form of dielectric relaxation should exist and polar clusters should freeze at low temperatures, similar to superparamagnetism. Following this idea, Viehland et al. proposed the "Dipolar Glass Model" analogous to magnetic spin glasses [148, 149]. They modelled dynamics of PNRs using the Vogel-Fulcher relation, which was originally given for a spin-glass system and is expressed as

$$f = f_0 \exp\left[-\frac{E_a}{k(T_{\max} - T_{VF})}\right] \tag{1.16}$$

where, f is the measurement frequency, f_0 is the attempt frequency, E_a is the activation energy, and T_{VF} is the Vogel-Flucher freezing temperature [149]. This proposed glass-like structure below the freezing temperature was later confirmed in PMN and PMN-PT using the heat capacity data. At temperatures below the freezing temperature, the thermal motion of the majority of PNRs is significantly reduced, and a long-range order can be established on the application of a suitable external field. The above-discussed models successfully explained relaxor behaviour in systems where charge disorder arises due to chemical inhomogeneity, such as $PbMg_{1/3}Nb_{2/3}O_3$ and $PbSc_{1/2}Nb_{1/2}O_3$. However, they failed to account for relaxor behaviour in systems with isovalent substitution, like Ba(Sn,Ti)O $_3$(BST) and Ba,(Zr,Ti)O_3 (BZT). To address this, Westphal et al. introduced the random field model [150]. According to this model, the non-ergodic phase of relaxors originates from a quenched random strain field (i.e., via homovalent cationic substitution). They further argued that replacing ferroelectric cations with non-ferroelectric cations induces polar entities (analogous to PNRs), which are surrounded by non-polar volume. The non-polar volume eventually hinders the individual dipoles from aligning collectively to

form a ferroelectric order. In BST and BZT, the distortion of TiO_6 octahedra depends on the chemical environment, i.e., concentration and type of dopants *viz.,* Sn^{+4} or Zr^{+4} ions at Ti^{+4} sites. The resulting relaxor state in $Ba(Sn,Ti)O_3$ and $Ba(Zr,Ti)O_3$ is primarily driven by the formation of random local strain fields, resulting in ferroelastic domain states. As an extension of the random field model, Glinchuk and Farhi (GF) proposed an order-disorder model for relaxors [145]. According to this model, relaxors consist of reorientable dipoles at high temperatures. These dipoles exist within a highly polarizable host lattice, which easily responds to electric fields. Generally, dipole-dipole interactions develop a ferroelectric (FE) order in the material at low temperatures. However, this model suggests that random local electric field disrupts a long-range ferroelectric order in relaxors. These fields can come from (a) static sources: chemical disorder, lattice vacancies, impurities, and other structural defects, and (b) dynamic sources: non-ferroelectric ions (ions that do not contribute to ferroelectricity) shifting from their ideal positions. Depending on the competitive interactions between the dipoles and degree of disorder, the material demonstrates different types of atomic ordering *viz.,* Ferroelectric (FE) state, Dipole Glass state, or mixed ferro-glass state. Another model proposed by Glazounov and Tagantsev provides a new theory for relaxors based on the motion of the boundaries between polar regions and the surrounding nonpolar matrix [151]. In contrast to traditional models, this model suggests that rather than reorienting, the boundaries of the PNRs shift(expand/contract) or "breathe" in response to the electric field, thereby influencing the dielectric response. In addition, several other models have been proposed to explain the relaxor behaviour in the context of the dynamics of polar nano-regions (PNRs) [125, 152, 153, 154, 155].

1.9 Literature review

1.9.1 Sodium Niobate ($NaNbO_3$): most complex perovskite

Sodium Niobate (NN) is one of the most studied perovskite material due to its complex structure and large number of structural phase transitions among different ferroic phases as a function of temperature [6, 69]. The distortions present in the various phases of NN are driven by cationic displacements and/or tilting of oxygen octahedra. Moreover, there are a large number of conflicting reports regarding the phase evolution of NN as a function of temperature [6, 69, 70, 156, 157, 158, 159]. Megaw showed that NN undergoes six structural phase transitions as a function of temperature, resulting into seven different crystallographic structures stable in different temperature ranges [69]. The phase transition sequence, as suggested by Megaw, is as follows:

Cubic (U) $[Pm\bar{3}m] \xrightarrow{913\,\mathrm{K}}$ Tetragonal (T2) $[F4/mbm] \xrightarrow{848\,\mathrm{K}}$ Orthorhombic (T1) $[Ccmm] \xrightarrow{793\,\mathrm{K}}$ Orthorhombic (S) $[Pnmm] \xrightarrow{753\,\mathrm{K}}$ Orthorhombic (R) $[Pnmm] \xrightarrow{633\,\mathrm{K}}$ Orthorhombic (P) $[Pbcm] \xrightarrow{173\,\mathrm{K}}$ Rhombohedral (N) $[F3c]$

Later, Darlington and Knight revisited the temperature-dependent evolution of NN and reported the unit cell multiplicities for different phases [158]. Some studies also suggested the presence of long-range modulated phases above room temperature using Dielectric, Raman, and Synchrotron X-ray diffraction data [160, 161]. Later on, Mishra et al. re-examined NN as a function of temperature and gave a new phase diagram (see Fig. 1.16) [6, 162]. The room temperature structure of $NaNbO_3$ is antiferroelectric (**P** phase) with *Pbcm* space group [cell size: $(\approx \sqrt{2}a_p) \times (\approx \sqrt{2}b_p) \times 4c_p)$] having a compound tilt system $(a^-a^-c^+)^2_1(a^-a^-c^-)^3_2(a^-a^-c^+)^1_3$, where a_p, b_p, and c_p are the parameters of basic cell [58, 59]. However, this antiferroelectric structure is very delicate and transforms into a ferroelectric structure with $Pmc2_1$ space group

on doping at A and/or B site or application of electric field [90, 163, 164]. Moreover, the low-temperature structure of NN is ferroelectric (space group: *R3c*; tilt system: $a^-a^-a^-$; cell size:$(\approx \sqrt{2}a_p) \times (\approx \sqrt{2}a_p) \times (\approx 2\sqrt{3}c_p)$ in hexagonal settings). Further, on heating above room temperature NN transits into **R** phase [space group: *Pbnm*; cell size: $(\approx \sqrt{2}a_p) \times (\approx \sqrt{2}b_p) \times 6c_p$], **S** phase [space group: *Pbnm*; cell size: $(\approx \sqrt{2}a_p) \times (\approx \sqrt{2}b_p) \times 12c_p$], **T1** phase [space group: *Cmcm*; tilt system: $a^0b^-c^+$; cell size: $(\approx 2a_p) \times (\approx 2b_p) \times 2c_p$], **T2** phase [space group: *P4/mbm*; tilt system: $a^0a^0c^+$ cell size:$\sqrt{2}a_p \times \sqrt{2}a_p \times c_p$], and finally transit into **U** phase [space group: $Pm\bar{3}m$; tilt system: $a^0a^0a^0$; cell size: $a_p \times a_p \times a_p$] [6]. Recently, neutron pair distribution analysis performed by Jiang et al. reveals that the local structure of $NaNbO_3$ below 490K is rhombohedral (space group: R3c), which is ferroelectrically distorted [36]. They also emphasize that the local domains in the ferroelectric structure (space group: *R3c*) have spontaneous polar alignment in antiparallel fashion which leads to the antiferroelectric structure (space group: *Pbcm* group) stable at room temperature [36]. In contrast, Htet et al. suggested that the local structure of NN at room temperature is

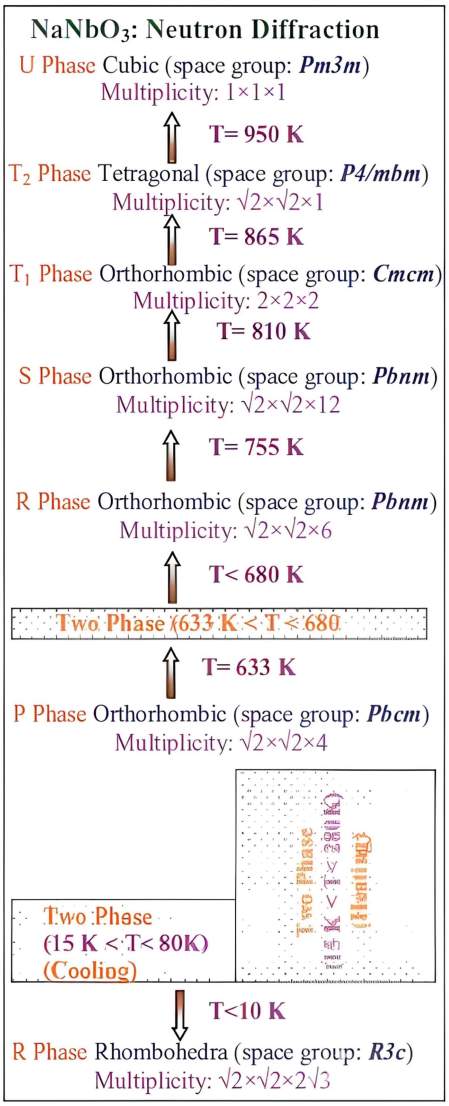

Fig. 1.16 Phase evolution of $NaNbO_3$ with temperature. The figure is adopted from ref. [6]

best described by orthorhombic phase with $Pmc2_1$ space group [165]. In addition, there are several other studies on NN that investigate structural phase transitions driven by pressure, electric field, particle size, etc. [166, 167, 168, 169]. The complex phase structures of $NaNbO_3$ are likely the primary reason why it serves as a fundamental compound for developing ferroelectric materials as alternatives to toxic, lead-containing materials. Moreover, in its pure form, it is utilised in high-density optical storage devices to improve nonlinear optical properties and as a material for holographic recording [18, 170, 171, 172].

1.9.2 Barium Titanate ($BaTiO_3$): first ferroelectric perovskite

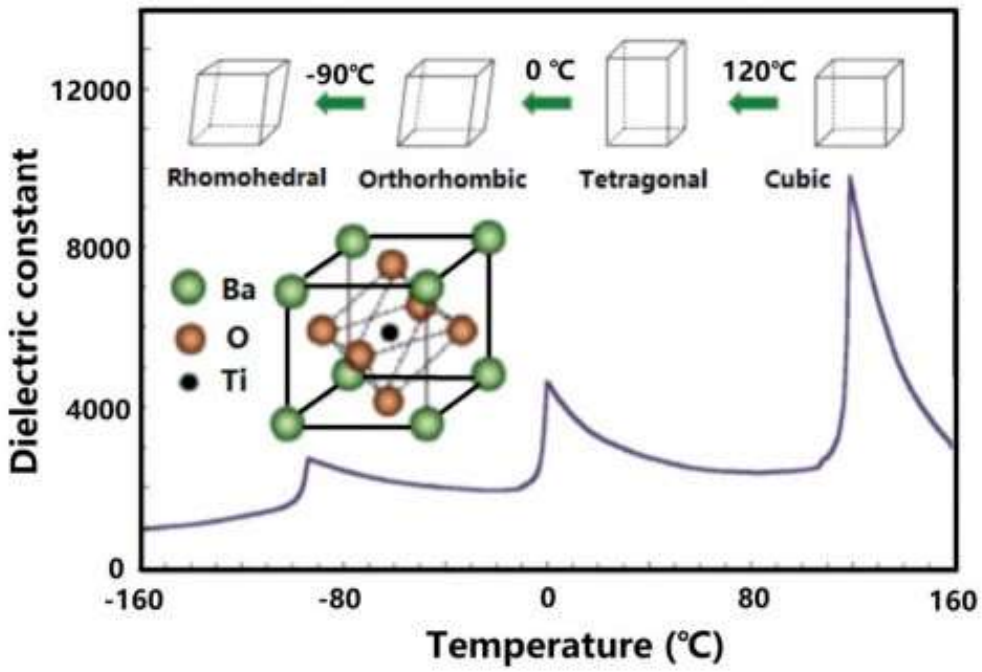

Fig. 1.17 Variation of real part of dielectric permittivity of barium titanate as a function of temperature [7].

Barium Titanate($BaTiO_3$) is one of the most extensively investigated ferroelectric material [9, 173, 174, 175]. Owing to its simple structure, it works as a model system to study the ferroelectric phenomenon in perovskites [9]. The ferroelectric behaviour of $BaTiO_3$ (BT) was independently discovered by von Hippel and his collaborators, as well

as by Wul and Goldmann, during the 1940s [176, 177]. The Curie temperature of Barium Titanate is ≈ 393 K [7]. Above this temperature, BT stabilizes in a perovskite-type (ABO_3) paraelectric (non-polar) structure with $Pm\bar{3}m$ space group. In this structure, the larger Ba cations sit at the corners of the cube, the smaller Ti cations sits at the body-centred positions, and the O anions occupy the face-centred positions. Barium Titanate undergoes three structural phase transitions as a function of temperature: Cubic (space group: $Pm\bar{3}m$) $\xrightarrow{\text{T = 393 K}}$ Tetragonal (space group: *P4mm*) $\xrightarrow{\text{T = 273 K}}$ Orthorhombic (space group: *Amm2*) $\xrightarrow{\text{T = 183 K}}$ Rhombohedral (space group: *R3m*) [178] (see Fig. 1.17). The ferroelectric phases of $BaTiO_3$ differ in the displacement direction and magnitude of the Ti cation, e.g., the Ti cations are displaced along the <100>, <110>, and <111> directions in tetragonal, orthorhombic, and rhombohedral phases, respectively (*R3m*) [73, 173]. On the other hand, rhombohedral symmetry has been reported at short ranges using neutron PDF, XAFS, XANES, etc., in all the structures (at long ranges) of BT, *viz.,* $Pm\bar{3}m$, *P*4*mm*, *Amm*2, and *R*3*m* [179, 180].

The long-range ferroelectric phase transitions in BT are generally described by two models *viz.,* displacive model [181, 182, 183] and order-disorder model [8, 73]. In the displacive model, the phase transitions are driven by the freezing of the ferroelectric zone-center phonon mode (Γ_4^-), associated with the Γ (q = 0,0,0) point of the cubic Brillouin zone [12]. Although, the primary order parameter driving these phase transitions is same (i.e., Γ_4^- irrep) yet the order parameter direction differs for each ferroelectric phase, e.g., (a,0,0) for *P4mm*, (a,a,0) for *Amm2*, and (a,a,a) for *R3m*. The order-disorder model of phase transitions proposed by Takahasi and Comes et al. provides a framework for understanding the ordering behaviour of Ti^{4+} cations in $BaTiO_3$ [73]. According to this model, the Ti^{4+} cations exhibit random off-centerd displacements within nanometer-sized regions, aligning in eight equivalent directions $\langle 111 \rangle$ in the cubic phase (see Fig. 1.18 (d)) [8]. As the system is cooled, these disordered displacements start to exhibit a degree of alignment,

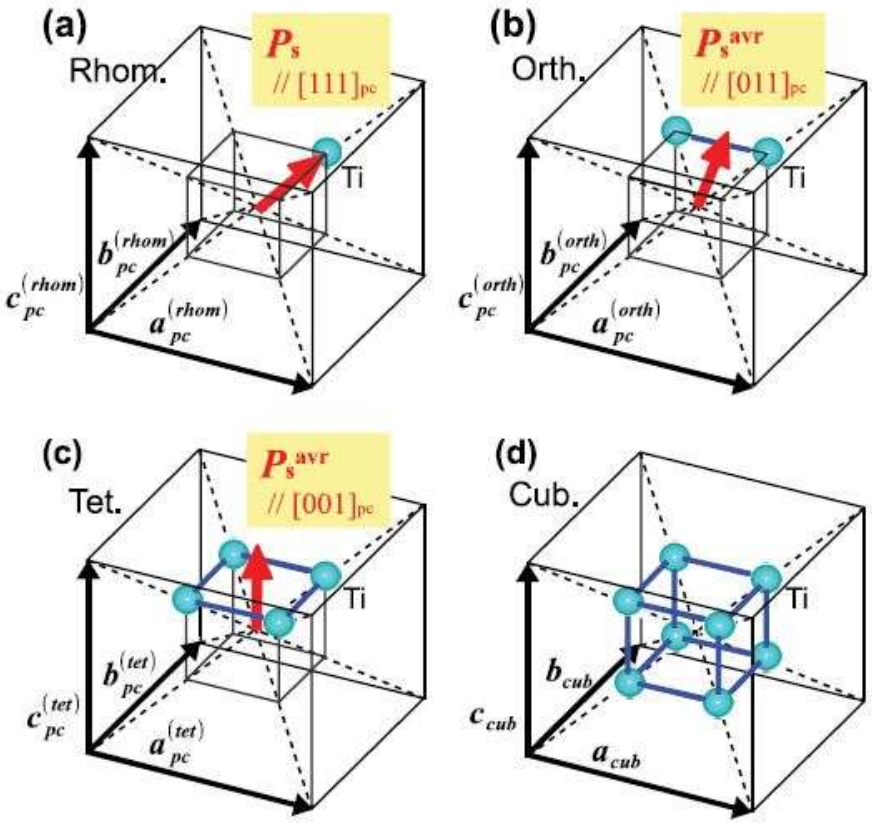

Fig. 1.18 Schematic representation of off-centered Ti atom along ⟨111⟩ directions in (a) rhombohedral, (b) orthorhombic, (c) tetragonal, and (d) cubic phases of $BaTiO_3$ [8].

with the Ti^{4+} cations preferentially orienting along four adjacent directions. This alignment marks the onset of the tetragonal phase, characterized by polarization along the ⟨100⟩ crystallographic directions (see Fig. 1.18(c)). Further cooling induces a greater degree of order, with the displacements aligning along two adjacent directions. This transition results in the orthorhombic phase, where the polarization vector shifts to the ⟨110⟩ direction (see Fig. 1.18(b)). At even lower temperatures, the displacements achieve complete order as they align along the ⟨111⟩ direction, leading to the formation of the rhombohedral phase. This phase represents the lowest temperature state of $BaTiO_3$, characterized by a completely ordered structure and polarization along the ⟨111⟩ direction (see Fig. 1.18(a)). Due to its high dielectric constant, BT is widely used in multilayer ceramic capacitors, sensors, actuators, and other applications [9, 19, 184]. However, despite many beneficial properties

of BT-based materials, their limited thermal stability has restricted their technological applicability.

1.9.3 Calcium Titanate ($CaTiO_3$)

Calcium Titanate ($CaTiO_3$) is a naturally occurring mineral that crystallizes in the orthorhombic perovskite structure at room temperature. It was first discovered in the Ural mountains of Russia by the German mineralogist Gustav Rose. $CaTiO_3$(CT) serves as the parent compound of the perovskite structural family. $CaTiO_3$(CT) is a quantum paraelectric material [185]. The structural phase transitions of $CaTiO_3$ have been extensively investigated [52, 186, 187, 188, 189, 190, 191, 192]. Vogt and Schmahl [191] reported a direct transition from the *Pbnm* phase to the $Pm\bar{3}m$ phase, with no intermediate phases between them. In contrast, some research groups [52, 186, 187, 188, 189, 190, 192] have reported the presence of one or more intermediate phases *viz., Cmcm*, *P4/mbm*, *I4/mcm* etc. between the *Pbnm* and high-temperature $Pm\bar{3}m$ phase. Now, it is well established that Calcium Titanate undergoes the following phase transition sequence: Cubic (space group: $Pm\bar{3}m$) $\xrightarrow{\mathbf{T = 1647\ K}}$ Tetragonal (space group: *I4/mcm*) $\xrightarrow{\mathrm{T = 1523\ K}}$ Orthorhombic (space group: *Pbnm*) [193]. It is important to note that all these phases exhibit a non-polar (paraelectric) state driven by in-phase/out-of-phase rotation of oxygen octahedra. Calcium Titanate is extensively utilized in electronic ceramic materials and for the immobilization of high-level radioactive waste [194, 195].

1.9.4 (Ba,Ca)TiO_3

Previous studies have shown that lead titanate ($PbTiO_3$) exhibits higher ferroelectric displacements in comparison to barium titanate ($BaTiO_3$) [38]. One of the key factors contributing to enhanced ferroelectricity is the higher tetragonal strain in $PbTiO_3$ (c/a = 1.06) as compared to $BaTiO_3$ (c/a = 1.01) [13, 196]. Significant efforts have been

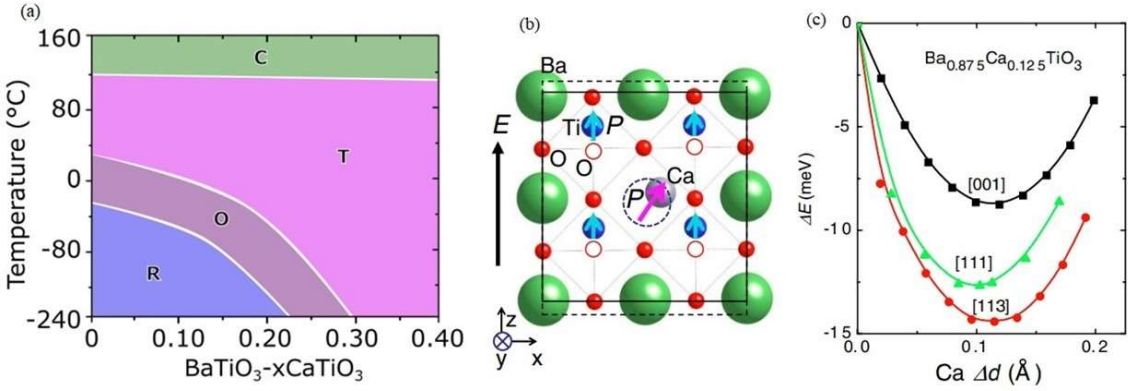

Fig. 1.19 (a) Phase diagram of $BaTiO_3$-$x$$CaTiO_3$ ceramics [9], (b) representation of off-centered calcium atoms in the tetragonal phase of $BaTiO_3$-$x$$CaTiO_3$ [10], and (c) the relative energies of $BaTiO_3$-$x$$CaTiO_3$; $x = 0.125$ for off-centered Ca atoms along [001], [111], and [113] directions [10].

made to modify the dielectric and ferroelectric properties of $BaTiO_3$-based materials, e.g., doping, microstructural modifications, via synthesizing thin films and nano-particles, etc. A-site substitution commonly involves alkaline-earth ions like Sr^{2+} or Mg^{2+}, as well as rare-earth ions such as La^{3+}, which tend to suppress Ti off-centering, consequently lowering the Curie temperature [197, 198, 199]. However, the influence of Ca-substitution in $BaTiO_3$ is notably different. The phase diagram of (Ba, Ca)TiO_3 (BCT) indicates that the incorporation of Ca in $BaTiO_3$ maintains the Curie temperature (T_c) while reducing the tetragonal-to-orthorhombic (T-O) and orthorhombic-to-rhombohedral (O-R) phase transition temperatures (see Fig. 1.19 (a)) [200]. As a result, BCT forms a tetragonal (*P4mm*) phase that remains stable for a broad temperature range [10]. The stability of the tetragonal phase increases with increasing Ca content. Theoretical predictions (later confirmed by various experimental studies) suggest that the smaller size of dopants at A-site promotes off-centering of the dopants, e.g., Ca^{2+} at Ba^{2+} site (see Fig. 1.19 (b)) [201, 202, 203]. Based on first-principles calculations for $(Ba_{0.875}Ca_{0.125})TiO_3$, Fu et al. observed that the Ca^{2+} cations off-centers along [113] direction, which do not conform to the constraints of either tetragonal or rhombohedral symmetry (see Fig. 1.19 (c)) [10].

Furthermore, off-centering of the ferroelectrically active Ca^{2+} cations enhances the off-centering of Ti^{4+} cations, in close analogy to the role of Pb^{2+} in promoting off-centering of Ti^{4+} cations in $PbTiO_3$ [202]. This off-centering results in a substantial increase in ferroelectric polarization of (Ba, Ca)TiO_3 [37].

1.9.5 (1-*x*) $NaNbO_3$ - *x* $BaTiO_3$

The solid solution of $NaNbO_3$ and $BaTiO_3$ (NN-*x*BT) has been extensively studied to identify compositions with enhanced physical properties [32, 33, 34, 35, 39, 42, 204, 205, 206, 207]. The initial efforts to construct a phase diagram for NN-xBT were made by Raveskii et al. in 1978 [204]. Their findings demonstrated the solubility of the NN in BT for the complete range [204]. Additionally, they reported a decrease in the temperature corresponding to the dielectric maximum up to $x = 0.60$, followed by an increase on further increasing the BT content. The highest dielectric response was observed at $x = 0.25$ by Raveskii et al. [204]. Interest in this solid solution was revived due to the ban on lead-based functional materials in the first decade of the 21st century. Zeng et al. conducted structural and electromechanical studies on this solid solution, focusing on the NN-rich region [35]. They reported a significant piezoelectric response for $x = 0.10$ having $d_{33} = 147$ pC/N and $k_p = 0.34\%$. This finding was subsequently corroborated by Xie et al. and Aoyagi et al., who also reported a Morphotropic Phase Boundary (MPB)-like enhancement in physical properties at $x \approx 0.10$ [39, 205]. Yamazoe et al. successfully fabricated thin films of NN-xBT with $x = 0.05$ and $x = 0.10$ [208]. They observed excellent crystallinity for the composition with $x = 0.10$, suggesting the potential for outstanding electromechanical properties. Research on NN-xBT with high compositions ($x > 0.25$) indicates relaxor behaviour, making it a promising candidate for ferroelectric energy storage applications [42, 206, 207]. Zuo et al. conducted strain versus field measurements on compositions located at the relaxor-to-ferroelectric boundary [40, 209]. They observed

a significant electrostrictive coefficient ($Q = 0.046$ m^4/C^2) for x = 0.25 [40, 209]. While the aforementioned studies primarily investigated the ferroelectric and dielectric properties of NN-xBT, they do not provide comprehensive structural studies. The first detailed structural investigations on the NN end of the NN-xBT ($0 \leq x \leq 0.20$) system were carried out by Jauhri et al. using temperature-dependent X-ray diffraction, neutron diffraction, and Raman spectroscopy [32, 33, 34]. Jauhri et al. identified the emergence of various antiferrodistorted phases as a function of temperature and composition. However, their synthesized samples exhibited impurity peaks in the diffraction patterns, with intensities comparable to those of the superlattice reflections, which could interfere with the accuracy of the structural information [32, 33, 34]. In a recent study, Wajahl et al. carried out temperature-dependent structural investigations on the Ca-substituted NN-x BT solid solution (NN-x BCT) [210, 211]. Their findings suggest the enhancement of ferroelectric properties on the incorporation of smaller Ca cations at Ba-sites. Considering the extensive research and the notable enhancement in electromechanical properties observed in the NN-xBT system, we have extended our investigation to a broader compositional range by exploring the solid solution of $NaNbO_3$ (NN) and $(Ba_{0.9}Ca_{0.1})TiO_3$ (BCT) i.e., (1-x)NN - xBCT within the entire composition range of $0 \leq x \leq 1$. This approach aims to gain a deeper understanding of the structure-property relationships and identify compositions exhibiting optimal functional properties useful for different technological applications.

1.10 Organisation of the thesis

The content of this thesis work has been organized as follows:

Chapter 2 describes the details of the sample synthesis and various characterization techniques.

Chapter 3 presents the synthesis and composition-dependent structural characterization of (1-x)$NaNbO_3$-x$(Ba_{0.9}Ca_{0.1})TiO_3$ (NN-xBCT) for $0.0 \leq$ x ≤ 1.0. The chapter involves a

comprehensive analysis using X-ray diffraction and Raman spectroscopy, complemented by dielectric measurements to investigate the structural and functional properties as a function of composition.

Chapter 4 focuses on the temperature-dependent multiscale structural analysis of a technologically significant composition, 0.9 $NaNbO_3$-0.1 $Ba_{0.9}Ca_{0.1}TiO_3$ (NN-10BCT). This study involves an integrated investigation using temperature-dependent synchrotron powder X-ray diffraction, Raman spectroscopy, and Pair Distribution Function (PDF) analysis to gain insights into the structural evolution across as a function of temperature. For this system, we have identified two unique Polymorphic phase boundaries *viz.,* (a) At ambient condition with coexisting *Amm2* & $Pmc2_1$ phases (b) At low temperatures with coexisting $Pmc2_1$ & *R3c* phases.

Chapter 5 presents the temperature-dependent Synchrotron X-ray diffraction, Raman spectroscopy, and PDF analysis of a lead-free realxor system 0.75 $NaNbO_3$- 0.25 $Ba_{0.9}Ca_{0.1}TiO_3$ (NN-25BCT). Moreover, we provide experimental science results on the influence of in-phase octahedral tilting on ferroelectricity in perovskites using an ingenious approach of mode crystallography for the very first time.

Chapter 6 presents an investigation of the anomalous thermal expansion and ferroelectrovolume effect in the relaxor system 0.40 $NaNbO_3$ - 0.60 $Ba_{0.9}Ca_{0.1}TiO_3$ (NN-60BCT). This study utilizes temperature-dependent synchrotron X-ray diffraction (SXRD) analysis alongside Pair Distribution Function (PDF) analysis. The observed volume contraction at low temperatures is attributed to the progressive correlations among short-range polar ordering.

Finally, **Chapter 7** provides a summary of the thesis work along with potential directions for future research.